# The Size, Structure and Ionization of the Broad Line Region in NGC 3227

Nick Devereux

*Department of Physics, Embry-Riddle Aeronautical University, Prescott, AZ 86301*

devereux@erau.edu

## ABSTRACT

*Hubble Space Telescope* (*HST*) spectroscopy of the Seyfert 1.5 galaxy, NGC 3227, confirms previous reports that the broad H$\alpha$ emission line flux is time variable, decreasing by a modest $\sim$ 13% between 1999 and 2000 in response to a corresponding $\sim$ 40% decrease in the underlying continuum. Modeling the gas distribution responsible for the broad H$\alpha$, H$\beta$ and H$\gamma$ emission lines favors a spherically symmetric inflow as opposed to a thin disk. Adopting a central black hole mass of $7.6 \times 10^6$ M$_\odot$, determined from prior reverberation mapping, leads to the following dimensions for the size of the region emitting the broad H$\alpha$ line; an outer radius $\sim$ 60 l.d and an inner radius $\sim$ 4 l.d. Thus, the previously determined reverberation size for the broad line region (BLR) consistently coincides with the inner radius of a much *larger* volume of ionized gas. However, the *perceived* size of the BLR is an illusion, a consequence of the fact that the emitting region is ionization bounded at the outer radius and diminished by Doppler broadening at the inner radius. The actual dimensions of the inflow remain to be determined. Nevertheless, the steady state mass inflow rate is estimated to be $\sim 1 \times 10^{-2}$ M$_\odot$ yr$^{-1}$ which is sufficient to explain the X-ray luminosity of the AGN in terms of radiatively inefficient accretion. Collectively, the results challenge many preconceived notions concerning the nature of BLRs in active galactic nuclei.

*Subject headings:* galaxies: Seyfert, galaxies: individual (NGC 3227), quasars: emission lines

## 1. Introduction

NGC 3227 is an early type SAB(s)a spiral galaxy located at a distance of 20.8 Mpc (Tully 1988). The galaxy harbors a Seyfert 1.5 nucleus (Ho, Filippenko, Sargent & Peng

1997) whose broad Balmer emission lines have long been known to be time variable. Since the broad line region (BLR) is unresolved, the spatial distribution of emission cannot be directly measured. However, reverberation mapping, which refers to measuring the time delay in the response of broad emission lines to time variable illumination from the central continuum source (Peterson 1993), has yielded a variety of estimates for the size of the broad line region (Peterson, Crenshaw & Meyers 1985; Winge et al. 1995; Peterson et al 2004; Kaspi et al. 2005; Denney et al. 2009, 2010). Even though the broad line emission emanates from a finite volume, reverberation mapping yields only a single size. Despite numerous attempts to model the reverberation phenomenon (e.g. Edelson & Krolik 1988; Robinson & Perez 1990; Welsh & Horne 1991; Horne, Peterson, Collier, & Netzer 2004, and references therein), the question remains *what exactly does the reverberation size refer to; the inner radius of the BLR or a luminosity weighted radius?*

Emission line profile fitting is a complementary technique used to constrain the physical dimensions of the BLR in low luminosity AGNs (LLAGNs) with known central masses. The merit of modeling LLAGNs is that they radiate well below the Eddington limit and are therefore unable to sustain a radiatively driven outflow. Consequently, gravity dominates the kinematics of the gas and the 3-D gravitational field strength is known by virtue of knowing the BH mass. Thus, the relationship between velocity and radius may be established, given a kinematic model for the gas. In this way one can exploit the exquisite velocity resolution of the Space Telescope Imaging Spectrograph (STIS) aboard the *Hubble Space Telescope* (*HST*) to model the broad emission line profiles and determine a shape and size for the BLR.

Large BLR size discrepancies are indicated for the LLAGNs M81, NGC 3998 and NGC 4203 (Devereux & Shearer 2007; Devereux 2011a,b). Specifically, the dimensions of the BLR deduced from emission line profile fitting are much larger than expected based on the reverberation size–UV luminosity correlation of Kaspi et al. (2005). However, Kaspi et al. (2005) note that the correlation appears to break down for AGNs with low UV luminosities, comparable to those measured for M81, NGC 3998 and NGC 4203, so the comparison may not be meaningful. On the other hand, the reverberation size has actually been measured for the LLAGN in NGC 3227, most recently by Denney et al. (2010). The principle aim of this paper, therefore, is to make the first direct comparison of the reverberation size with the dimensions of the BLR in NGC 3227 deduced from emission line profile fitting. The larger context for this investigation is to understand why it is that BH masses estimated using the reverberation radius require a considerable factor of $\sim 5.5$ correction in order to place the them on the $M_\bullet$–$\sigma_*$ relation defined by BH masses measured directly using gas kinematics and stellar dynamics (Onken et al. 2004).

The mass of the BH in NGC 3227 has been measured using three different methods;

stellar dynamics (Davies et al. 2006), gas kinematics (Hicks & Malkan 2008) and most recently via reverberation mapping (Denney et al. 2010), collectively yielding mass estimates in the range $(0.7 - 2) \times 10^7$ $M_\odot$. When combined with the X-ray luminosity the range of BH masses indicate that NGC 3227 is radiating at $\leq$0.4% of the Eddington luminosity limit (Winter, Veilleux, McKernan & Kallman 2011; Xu 2011; Vasudevan & Fabian 2009).

The layout of the paper is as follows. In Section 3, the broad emission lines seen in NGC 3227 are evaluated in the context of inflow and accretion disk models. Some physical properties of the BLR are presented in Section 4 including the size, structure and source of ionization. Conclusions follow in Section 5. We begin, however, with Section 2 and a review of the emission lines observed in the nucleus of NGC 3227.

## 2. NGC 3227 Emission Lines

NGC 3227 has been observed with STIS twice; once in 1999 with the G750M grating and again in 2000 with the G750L, G430L, G230L and G140L gratings. Table 1 summarizes the observations and the archival spectra are presented in Figure 1. STIS spectra showing the UV–visible emission have been presented previously; Crenshaw, Kraemer, Bruhweiler, & Ruiz (2001) based on observations obtained under PID 8479 and the G750M spectrum obtained under PID 7403, by Walsh et al. (2008). All spectra shown in the following refer to a 7 pixel wide extraction along the slit direction and centered on the nucleus. Each extraction samples $\geq$ 80% of the encircled energy for an unresolved point source (Proffitt et al. 2010).

The G750M spectrum reveals a broad H$\alpha$ line with a FWHM $\sim$ 2000 km/s. Two narrow but resolved [O I] lines appear on the blue side of the broad H$\alpha$ line at $\sim$ 6350Å and two narrow but resolved [S II] lines appear on the red side at $\sim$ 6750Å. The narrow [S II] lines are not resolved in the G750L spectrum but their combined flux is the same, within the measurement uncertainties, as in the G750M spectrum obtained in 1999. In contrast, the broad H$\alpha$ line decreased in brightness by a modest $\sim$ 13% between 1999 and 2000 in response to a corresponding $\sim$ 40% decrease in the underlying continuum. Collectively, the G750M, G750L and G430L spectra resolve the H$\alpha$, H$\beta$ and H$\gamma$ lines, a more detailed description of which follows in the next section.

### *2.0.1. Broad Hα Emission*

The H$\alpha$ emission line profile is single peaked and both of the [N II] vacuum wavelength 6549.85 and 6585.28 Å emission lines and the narrow component of the vacuum wavelength 6564.61 H$\alpha$ emission line can be seen in the G750M spectrum which greatly facilitates their modeling. The **STSDAS** contributed task **specfit** was used to model and subtract the forbidden lines and the results are reported in Table 2 along with the fluxes for the two [S II] vacuum wavelength $\lambda$6718.29 and $\lambda$6732.67 Å emission lines and the two [O I] vacuum wavelength $\lambda$6302.04 and $\lambda$6365.53 Å emission lines. The flux for the model [N II] lines and the model *narrow* H$\alpha$ line has been chosen so that the difference spectrum does not show an 'over-subtraction' of the broad H$\alpha$ profile. The procedure is valid because the observed broad H$\alpha$ emission line profile is otherwise smoothly varying. In support of the procedure, the model parameters deduced for the [N II] lines are consistent with the expectation based on atomic physics that sets the wavelength of the fainter [N II] line relative to the brighter [N II] line, constrains the flux of the fainter [N II] line to be 1/3 that of the brighter [N II] line and requires that the [N II] lines share the same width, chosen to be the same as measured for the brightest [O I] line. Two components were required to model the brightest [N II] line in order to obtain a satisfactory subtraction as noted in Table 2. A single gaussian was used to model the other lines. That these forbidden lines have similar widths and further that the narrow H$\alpha$ line is fainter than the brightest [N II] line are characteristics shared by other AGNs observed with STIS for which these lines can be clearly seen (Noel–Storr et al. 2003).

A model narrow line spectrum is illustrated in Fig. 2 along with the difference spectrum revealing a broad H$\alpha$ line whose profile is symmetric about the $\lambda$6588Å wavelength expected for a systemic velocity of 1126 km/s deduced from the peak of the brightest [N II] emission line. Thus, there is no apparent redshift between the broad H$\alpha$ emission line and the systemic redshift of the host galaxy. The forbidden line model produced using the G750M spectrum is also adopted for the lower resolution G750L spectrum, motivated by the observation that the flux in the two [S II] lines did not change between 1999 and 2000. Figure 2 illustrates that the consequence of subtracting the forbidden emission line model is to reveal a broad H$\alpha$ emission line that is very similar to the H$\beta$ line described in the next section. The broad H$\alpha$ emission line flux in the 1999 G750M spectrum is $\sim$ 13% larger than measured in the 2000 G750L spectrum (see Table 2).

### *2.0.2. Broad Hβ and Hγ Emission*

The H$\beta$ and H$\gamma$ emission lines are compromised only slightly by [O III] emission lines which were modeled and subtracted using the **STSDAS** contributed task **specfit** as illustrated in Fig. 3 and Fig. 4. The [O III] vacuum wavelength $\lambda$4364.44 Å deserved special attention as it is very faint and marginally resolved. A model was employed for the [O III] $\lambda$4364.44 line in which the wavelength and line width was fixed and the flux adjusted so as to not over-subtract the H$\gamma$ line in the difference spectrum. This yielded the upper limit for the [O III] $\lambda$ 4364.44 line reported in Table 3. Subtracting the [O III] lines reveals broad H$\beta$ and H$\gamma$ emission lines. Unfortunately, the analysis can not reliably be extended to include other Balmer lines as they are even fainter and even more confused with emission from other ions. Consequently, emission line fluxes are reported in Table 3 for all the lines that can be reliably resolved and measured in the G430L spectrum including H$\beta$, H$\gamma$, the two [O III] vacuum wavelength $\lambda$4960.30 Å and $\lambda$5008.24 Å emission lines and the upper limit for the vacuum wavelength $\lambda$4364.44 Å [O III] emission line. The [O II] $\lambda\lambda$3727.09, 3729.88 lines are so faint and the H$\alpha$ line so bright that the [O III] $\lambda$5008.24 /[O II] $\lambda\lambda$3727.09, 3729.88 and [O I] $\lambda$6324.99/H$\alpha$ emission line ratios measured with STIS locate NGC 3227 outside the boundaries of the Kewley et al. (2006, their Fig. 5) diagnostic diagram. Consequently, the STIS spectra render the AGN in NGC 3227 unclassifiable.

### *2.0.3. Balmer Decrements*

The observed Balmer decrements, H$\alpha$/H$\beta$ = 4.0 $\pm$ 0.01, slightly lower than the value of $\sim$5 reported previously using ground based telescopes (Winge et al. 1995; Cohen 1983), and H$\beta$/H$\gamma$ = 3.2 $\pm$ 0.02, measured for the first time with STIS, are both significantly different from the Case B values, 2.75 and 2.1, respectively, in the sense that the observed values are systematically 45% and 52% higher, respectively. Deviations from recombination theory have been noted for other AGNs (e.g. Devereux 2011a,b; Storchi-Bergmann et al., 1997; Bower et al. 1996; Filippenko & Hapern 1984) and have been attributed to collisional excitation in gas of high density and temperature rather than dust extinction. Indeed, the striking similarity between the H$\alpha$, H$\beta$ and H$\gamma$ lines illustrated in Figure 5, when they are normalized to their respective peak intensities and the wavelength scales converted to velocity using the non-relativistic Doppler equation, suggests that the dust extinction to the BLR in NGC 3227 is negligible.

## 3. BROAD LINE REGION MODELS

NGC 3227 is unable to sustain a radiatively driven outflow (e.g. Fabian, Celotti, & Erlund 2006; King & Pounds 2003; Murry & Chiang 1997; Shlosman, Vitello, & Shaviv 1985) because the AGN radiates at $\leq 4 \times 10^{-3}$ the Eddington luminosity limit (Winter, Veilleux, McKernan & Kallman 2011; Xu 2011; Vasudevan & Fabian 2009). However, single peak broad Balmer emission lines, similar to those observed in NGC 3227, can be produced by an inflow (e.g. Devereux 2011a) or an accretion disk (e.g. Eracleous & Halpern 2001) and both models are tested in the following.

### 3.1. Central Stellar Mass

In an inflow or disk model the velocity law is determined by the central mass distribution, M(r), which can be modeled as a point mass, $M_\bullet$, representing the BH, embedded in the center of an extended star cluster. The central stellar mass may be important given the relatively low mass estimated for the BH in NGC 3227. Hicks & Malkan (2008) conveniently parameterize the $H$-band surface brightness profile of NGC 3227 in terms of a Sérsic function which may be integrated to determine the line-of-sight, or projected, luminosity in a variety of synthetic apertures. Such projected luminosities can be converted into central masses using the mass-to-projected-light ratio provided in Devereux, Becklin & Scoville (1987). Following this methodology leads to the values presented in Table 4 which, when compared to estimates of the central stellar mass density presented previously by Davies et al. (2006, their Figure 15), reveals a very large discrepancy. For example, the first row in Table 4 corresponds to an angular radius of $\sim 0.01''$ inside which the stellar mass density is estimated to be $\sim 1.3 \times 10^6 \mathrm{M}_\odot/\mathrm{pc}^3$. This is $\sim$ 15,000 times smaller than the value estimated by Davies et al. (2006) inside that same radius. The reason for the difference has not been determined. Consequently, the values presented in Table 4 are adopted in the following analysis.

### 3.2. Inflow Model

The spherically symmetric inflow model has been described most recently by Devereux (2011a) and employs a steady-state free-fall of *discrete* particles. Consequently, the model is *not* a Bondi flow (Bondi 1952). A discrete particle model is favored because of its ability to reproduce the small scale structure observed for broad emission line profiles (e.g., Capriotti, Foltz & Byard 1981). The velocity law and mass conservation determine the number density of inflowing particles to be $n(r) \propto r^{-3/2}$. Consequently, there are only two

free parameters; the inner and outer radii of the inflow, $r_i$ and $r_o$, respectively. Values that produce a reasonable representation of the broad Balmer emission line profiles observed for NGC 3227, shown in Figure 5, correspond to an outer radius, $r_{outer} = 1.3 \times 10^5 r_g$, and an inner radius, $r_{inner} = 9.3 \times 10^3 r_g$, where $r_g = GM_\bullet/c^2$, the gravitational radius.

### 3.3. Relativistic Accretion Disk Model

The disk model, presented by Chen & Halpern (1989), describes the emission line profile expected from a thin axisymmetric, relativistic accretion disk. The model includes self-consistently all relevant relativistic effects, such as Doppler boosting and transverse and gravitational redshifts and involves five free parameters. Values of the parameters that best reproduce the Balmer line profiles observed for NGC 3227, shown in Figure 5, are a dimensionless outer radius, $\xi_o = 3.5 \times 10^5 r_g$, an inner radius, $\xi_i = 2.5 \times 10^3 r_g$, an inclination angle measured from the disk normal to the line of sight, $i = 50^\circ$, an emissivity law of the form $r^{-q}$, where $q = 2$ and a velocity dispersion for the gas, $\sigma = 300$ km/s.

Interestingly, Figure 5 illustrates that the broad Balmer line profile shapes can be represented equally well by an inflow or an accretion disk; the reduced $\chi^2 \sim 12$ for both models. The effective velocity resolution of the model profiles is $\sim 230$ km/s, similar to that of the G750L grating and about twice that of the G430L grating. In either case the residuals between the observed profiles and the model are $\leq 10\%$ except for the fainter and consequently noisier H$\gamma$ line profile. Both the disk and inflow models have a similar shortfall in that they both predict slightly less emission on the blue side of the profile than is observed.

### 3.4. The Importance of Spectral Resolution

Figure 6 shows the broad H$\alpha$ line measured with the higher resolution G750M grating. Significant features are revealed including a bright central spike that is easily reproduced by the model inflow, for which the reduced $\chi^2 \sim 7$, but is not reproduced at all well by the disk model, which has a reduced $\chi^2 \sim 16$. The only difference between the models shown in Figure 5 and Figure 6 is that the effective velocity resolution of the model profiles presented is higher, $\sim 27$ km/s and comparable to the G750M grating. The superior ability of the inflow model to realistically reproduce broad emission lines observed at different spectral resolutions highlights a shortcoming of the Chen & Halpern (1989) disk model.

Real broad emission lines exhibit significant structure in their profiles, particularly at high spectral resolution, suggesting the combined emission of several thousand *discrete emit-*

*ters*. Historically, the widely quoted *optically thick broad line cloud* model found early support by accounting for such irregularities (e.g., Capriotti, Foltz & Byard 1981). The *optically thick broad line cloud* model remains popular to this day, even though the origin and confinement of such *clouds* is a major unsolved problem (Mathews & Ferland 1987). With hindsight, it may be more realistic to identify the *clouds* with *filaments*, motivated by the observation that ionized, density bounded gas filaments are commonly seen in the nuclei of active galaxies (Storchi-Bergmann 2009) including the Galactic center (Lacy, Achtermann & Serabyn, 1991). Such filaments have approximately the same gas density and hence the same emissivity regardless of their location with respect to the central AGN, they are optically thin, emit isotropically and have a very low volume filling factor. As noted by Capriotti, Foltz & Byard (1981), irregularities in the broad line profile result from statistical clumping of discrete emitters in radial velocity, as illustrated in Figures 7 and 8 for the inflow model. Detecting such irregularities depends on the number of filaments and the spectral resolution of the detector. The irregularities clearly seen in the broad H$\alpha$ emission line of NGC 3227 observed with the G750M grating are mimicked by the inflow model and suggest that the inflow is illuminated by the collective emission of $\sim 10^4$ ionized gas *filaments*. On the other hand, the inability of the Chen & Halpern (1989) disk model to reproduce the details of the broad H$\alpha$ emission line observed with the G750M grating is a limitation of the model that can be overcome by employing a *discrete* accretion disk model, described in the next section.

### 3.5. Discrete Non-relativistic Accretion Disk Model

In the discrete non-relativistic[1] accretion disk model the relationship between velocity and radius is determined by the mass distribution, *M(r)*, to be

$$v(r) = -\sqrt{GM(r)/r} \tag{1}$$

where *M(r)* is as described in Section 3.1. In a spherical coordinate system, the observed radial component of the velocity for a particle at position $(r, \theta)$, is given by

$$v_o = v(r)\ sini\ cos\theta \tag{2}$$

where $0 \leq \theta \leq 2\pi$ and $i$ is the angle of inclination measured from the disk normal to the line of sight.

[1]A discrete *relativistic* disk model is beyond the scope of the present paper.

As illustrated in Fig. 7, a model broad line profile, $\Phi(v)$, may be produced by generating a histogram of observed velocities $\{v_{o,i}\}$ for a system of particles indexed by $i$ and distributed randomly within a disk

$$\Phi(v) = \#\{i | v \leq v_{o,i} \leq v + dv\}. \tag{3}$$

Here $v_{o,i}$ denotes the observed velocity of the $i^{th}$ particle. Implicit in this model is the assumption that the particles share the same emissivity and emit isotropically. The distribution of points is used to produce a broad line profile by creating a series of concentric rings $\{R_j\}$ of radii $\{r_j\}$ selected randomly between $r_{inner}$ and $r_{outer}$. On each ring, $\{R_j\}$, there are $N(r_j)$ particles where

$$N(r) \propto r^{-q}. \tag{4}$$

distributed randomly in position angle, $\theta$. Each model profile employs a total of $\sim 10^4$ points. The resulting velocity histogram is binned by 25 km/s and subsequently smoothed using a 40 bin moving average. The resulting model velocity resolution is comparable to that of the G750L spectrum, shown in the left hand panel of Figure 7. The two emission peaks, a distinguishing characteristic of disk models, may be merged into a single peak and the profile wings made symmetric if the disk has a large outer radius and is inclined to the line of sight. The model also incorporates a 250 km/s velocity dispersion to widen the two velocity peaks so that they merge into a reasonable representation of the single peak seen in NGC 3227. Additionally, the model incorporates a value for q=0.5 which accentuates emission from the inner regions of the disk. Values for the parameters that best reproduce the G750L spectrum are very similar to those employed for the relativistic accretion disk model described in section 3.2; an outer radius, $r_{outer} = 1.3 \times 10^5 r_g$, and an inner radius, $r_{inner} = 9.3 \times 10^3 r_g$, where $r_g = GM_\bullet/c^2$, the gravitational radius, and an inclination, $i = 50°$. However, unlike the relativistic accretion disk model of Chen & Halpern (1989), the line profile shape produced by the discrete accretion disk model is also sensitive to the effective velocity resolution. When the velocity resolution of the model profile is increased by a factor four to match the G750M spectrum[2], shown in the right hand panel of Figure 7, the profile resolves two peaks, in stark contrast to the observed spectrum which exhibits only a single peak. Thus, on the basis of modeling the higher resolution G750M spectrum, it appears that the broad Balmer line profiles observed in NGC 3227 are unlikely to be produced by an accretion disk.

[2]holding the disk parameters fixed at the values used to model the G750L spectrum.

## 4. Discussion

The exquisite spectra obtained for NGC 3227 with the *HST* reveal an important observational phenomenon; that the shape of its bright and broad H$\alpha$ line changes with the resolution of the grating employed to observe it, as expected if the emission line is produced by thousands of discrete emitters as explained previously by Capriotti, Foltz & Byard (1981). Furthermore, the bright central spike observed for the line using the high resolution G750M grating is inconsistent with the profile shape expected for an accretion disk. Whereas it is already known that the velocity field of the narrow line gas in NGC 3227 is chaotic (Walsh et al. 2008, and references therein), the symmetry of the broad H$\alpha$ line suggests a rather ordered velocity field, demonstrably consistent with an inflow, the size, structure and ionization of which is explored further in the following.

### 4.1. Broad Line Region Ionization

The ionizing continuum generated by the AGN in NGC 3227 may be represented, in the year 2000, as a power law with an optical to X-ray spectral index $\alpha = 1.17$ (Vasudevan & Fabian 2009) and a normalization provided by the extinction corrected UV continuum described in Section 4.2. Integrating the spectral energy distribution from 13.6 eV to 100 keV using the method described previously in Devereux (2011a) predicts $6.1{\times}10^{52}$ ionizing ph/s. For comparison, the broad H$\alpha$ emission line flux measured in the year 2000 (Table 2) corresponds to an H$\alpha$ luminosity, $L(H\alpha) = 2.4{\times}10^{7}$ L$_{\odot}$, which, assuming 45% of the ionizing photons are converted into H$\alpha$ photons (Case B recombination at a temperature of $10^4$ K) requires $6.8{\times}10^{52}$ ionizing ph/s using,

$$N_{ion} = L(H_{\alpha})\alpha_B/\alpha_{H\alpha}^{eff} h\nu_{H\alpha} \tag{5}$$

where $\alpha_{H\alpha}^{eff}$ = 1.16 x $10^{-13}$ cm$^3$ s$^{-1}$ is the effective recombination coefficient and $\alpha_B$ = 2.59 x $10^{-13}$ cm$^3$ s$^{-1}$ is the total Case B recombination coefficient.

The comparison shows that the number of ionizing photons required to excite the broad H$\alpha$ emission line measured in the year 2000 coincides with the number of ionizing photons available from the AGN in that same year to within $\sim 10\%$[3] which is considered to be good, possibly fortuitous, agreement given the large extinction correction and the known UV and X-ray variability (Makowitz et al. 2009; Vasudevan & Fabian 2009). Nevertheless, the

[3]independent of the gas density and the filling factor.

comparison suggests that the central AGN is apparently able to ionize the entire BLR in NGC 3227 which necessarily entails a high, $\sim 100\%$, covering factor. Such a high covering factor is easy to achieve with a spherical distribution of gas and impossible to achieve with a thin accretion disk, further favoring an inflow as the origin of the broad Balmer emission lines seen in NGC 3227.

### 4.2. BLR Size

Kaspi et al. (2005) noted that NGC 3227 does not conform to the correlation between reverberation size and UV luminosity established for quasars and high luminosity AGNs. However, Crenshaw, Kraemer, Bruhweiler, & Ruiz (2001) present evidence for considerable dust extinction to the central UV source in NGC 3227 amounting to $\sim 4.3$ mag at 1450Å. The consequence of matching the extinction corrected 1450Å UV luminosity, estimated using Figure 1 to be $1.65 \times 10^{42}$ erg s$^{-1}$, with the smaller reverberation size measured by Denney et al. (2009, 2010) is to translate NGC 3227 closer to the correlation defined by quasars and high luminosity AGNs thereby reducing the discrepancy first noted by Kaspi et al. (2005).

Adopting a BH mass allows the gravitational radii determined using the inflow model (Section 3) to be converted into a physical size. If one adopts the reverberation BH mass of $7.6 \times 10^6$ M$_\odot$ (Denney et al. 2009, 2010), then the inner and outer radii of the model inflow correspond to $r_i \sim 4$ l.d and $r_o \sim 60$ l.d, respectively. Thus, the inner radius of the inflow model consistently coincides with the reverberation radius ($3.8 \pm 0.8$ l.d.) reported by Denney et al. (2009, 2010). The most straightforward interpretation of this result is that reverberation mapping locates just the inner radius of a much larger volume of ionized gas. Presumably, reverberation mapping locates the inner radius because this is where the number density of inflowing gas filaments is highest and the gas density in the filaments is also highest as explained in Section 4.4, but the emission is inevitably diminished *in a spectrum* to zero intensity for smaller radii by an ever increasing Doppler spread. Thus, the inner radius is actually an illusion. Since the emitting region is ionization bounded, the notion of an outer radius is also an illusion. Consequently, what we perceive as the BLR in NGC 3227, visualized in Figure 8, is just the illuminated shell of a much larger volume of inflowing gas whose actual dimensions remain to be determined. A measure of the inflow rate can be judged from the animation presented in Figure 8 which shows that the inflowing gas moves from the reverberation radius, $\sim 4$ l.d., into the BH in $\sim 7$ months.

### 4.3. Virial Black Hole Masses

The virial product of reverberation radius, $R$, and the velocity width[4] of the broad Balmer line, $\Delta V$, leads to a BH mass according to the relation;

$$M_\bullet = f R \Delta V^2 / G \tag{6}$$

where $f$ is a correction factor that locates the reverberation BH masses on the $M_\bullet$–$\sigma_*$ relation defined by BH masses measured directly using gas kinematics and stellar dynamics. $f$ has a value of $\sim 5.5$ (Onken et al. 2004). However, if the broad Balmer lines *are* produced by an inflow then it follows that the reverberation radius corresponds to the inner radius of the flow. Figure 8 visualizes the model inflow and identifies 8% of the broad H$\beta$ line flux that is observed to be time variable[5] (Winge et al. 1995; Denney et al. 2009, 2010). Figure 9 illustrates that the inner edge of the inflow defines the full width at zero intensity for the broad emission line profile. Consequently, the correct virial product, at least for NGC 3227, is the reverberation radius (0.0035 pc) and the half width at zero intensity (4300 km/s) squared. Then one recovers the reverberation BH mass of $7.6 \times 10^6$ $M_\odot$ with $f = 1$. Thus, there is no need for the correction factor, $f$, if the virial product utilizes a radius with the maximum velocity measured *at that same radius*.

### 4.4. Constraints on the Inflow Gas Density and Temperature

The [S II] lines have a line width corresponding to 360 km/s indicating that they arise from gas at a radial distance of $\sim 0.5$ pc. Thus, the two [S II] lines provide an opportunity to measure the gas density well beyond the portion of the inflow that is ionized by the central AGN. The nominal value for the observed [S II] $\lambda6742/\lambda6757$ intensity ratio $= 0.78 \pm 0.05$, corresponding to n $= 10^3$ cm$^{-3}$. The fact that the FWHM of the broad Balmer emission lines is larger than that of the [O I] and [O III] emission lines (Table 2 & 3) suggests that the gas density *inside* the inflow must be greater than the critical density of the levels from which the [O I] and [O III] lines originate which is $\sim 10^6$ cm$^{-3}$. This limit is higher than the one obtained from the [S II] line ratio implying that the gas density increases towards the central BH.

---

[4]the FWHM or the second moment(Collin, Kawaguchi, Peterson & Vestergaard 2006)

[5]The H$\alpha$ variability amplitude is observed to be $\sim 13\%$ with STIS. However, adopting 13% of the flux as the time variable component does not change the visual impression depicted in Figure 8 that reverberation mapping locates just the inner edge of a much larger volume of gas.

The limit for the observed [O III] ratio ($\lambda$4960.30 + $\lambda$5008.24) / $\lambda$4364.44 $\geq$ 34 yields T $\leq$ 10,400 K for the electron temperature if $n = 10^6$ cm$^{-3}$, which is judged to be representative of the temperature *inside* the BLR because the vacuum wavelength [O III] $\lambda$4960.30 and $\lambda$5008.24 lines are observed to have a FWHM $\sim$ 1600 km/s corresponding to a radius of 0.026 pc which places the [O III] emitting region inside the inflow.

The ionization parameter, $\Gamma$, given by

$$\Gamma = N_{ion}/4\pi r^2 c\ n \tag{7}$$

corresponds to $7 \leq \Gamma \leq 1994$ for gas inside the BLR with $0.05 \geq r(\mathrm{pc}) \geq 0.003$ pc and ionized by the central AGN. Such values for the ionization parameter are similar to those expected inside an HII region ionized by an O5 star. That is not to say that the ionization in NGC 3227 is provided by O5 stars, but rather that the electron temperature is expected to be similar and consistent with the limit $\leq$ 10,400 K determined from the [O III] ratio ($\lambda$4960.30 + $\lambda$5008.24) / $\lambda$4364.44.

### 4.5. The Mass of Ionized Gas Required to Produce the Broad H$\alpha$ Emission Line

The mass of emitting gas may be deduced from the broad H$\alpha$ emission line luminosity assuming standard (Case B) recombination theory;

$$M_{emitting} = L(H\alpha)m_H/\mathrm{n}\alpha^{\mathrm{eff}}_{\mathrm{H}\alpha}\mathrm{h}\nu_{\mathrm{H}\alpha} \tag{8}$$

Using an effective recombination coefficient $\alpha^{eff}_{H\alpha} = 1.16$ x $10^{-13}$ cm$^3$ s$^{-1}$, assuming a *constant* average density n $\geq 10^6$ cm$^{-3}$, and a luminosity $L(H\alpha) = 2.4$ x $10^7$ L$_\odot$ based on the broad line flux measured in 2000 (Table 2), leads to an upper limit on the mass of inflowing ionized gas, $M_{emitting} \leq 222$ M$_\odot$. If only a fraction of the gas is ionized then the upper limit on the *total* (ionized + neutral) gas mass could, of course, be higher.

### 4.6. An Assessment of the Inflow Scenario for NGC 3227

Once the dimensions of the emitting region have been established it is straight forward to calculate the volume filling factor, $\epsilon$, for the ionized gas producing the H$\alpha$ emission. For a uniform density medium occupying a spherical volume of radius $r$, one finds

$$\epsilon = 3L(H_\alpha)/4\pi \mathrm{n}_\mathrm{H}^2 \alpha_{\mathrm{H}\alpha}^{\mathrm{eff}} \mathrm{h}\nu_{\mathrm{H}\alpha} \mathrm{r}^3 \quad (9)$$

Again, using an effective recombination coefficient $\alpha_{H\alpha}^{eff} = 1.16 \times 10^{-13}$ cm$^3$ s$^{-1}$, assuming a *constant* average number density n $\geq 10^6$ cm$^{-3}$, and a luminosity $L(H_\alpha) = 2.4 \times 10^7$ L$_\odot$ based on the measurement of the broad line flux reported in Table 2 for the year 2000, leads to an upper limit on the filling factor, $\epsilon \sim 1$, for NGC 3227 if the size of the inflow, $r = 0.06$ pc. The very high filling factor indicates that the emitting volume is essentially completely filled with ionized gas.

Having established the dimensions of the emitting region and a lower limit on the gas density one can estimate the mass inflow rate, $\dot{m}$, for the ionized gas observed in the year 2000, using the equation of continuity;

$$\dot{m} = \epsilon 4\pi r^2 \mathrm{vnm}_\mathrm{H} \quad (10)$$

The free-fall velocity, v, at the inner radius, 0.003 pc, is determined by the central mass to be 4748 km/s. Setting $\epsilon = 1$ for a self-consistent gas density in the flow of n = $10^6$ cm$^{-3}$ (see section 4.4), leads to a mass inflow rate, $\dot{m} \sim 1.2 \times 10^{-2}$ M$_\odot$ yr$^{-1}$. However, if only a fraction of the inflowing gas is ionized, then the *total* mass inflow rate could, of course, be higher.

For comparison, the 2-10 keV X-ray luminosity measured for the AGN in the year 2000, $L_{2-10\ keV}$, is $3.2 \times 10^{41}$ erg s$^{-1}$ (Vasudevan & Fabian 2009). Assuming this is powered by radiatively inefficient accretion leads to the following formula (Merloni, Heinz, & Di Matteo 2003)

$$L_{2-10\ keV} = 7 \times 10^{38} M_\bullet^{0.97} \dot{m}^{2.3} \quad (11)$$

where $L_{2-10\ \mathrm{keV}}$ is in $erg\ s^{-1}$ and $M_\bullet$ is in solar masses. Under these circumstances the accretion rate required to power the observed X-ray emission, $\dot{m} \sim 1.8 \times 10^{-2}$ M$_\odot$ yr$^{-1}$, is comparable to the mass inflow rate inferred from the broad H$\alpha$ line emission seen in the same year.

### 4.7. Accretion Problem Solved?

There are two major unsolved problems with regard to fueling AGN. The first is why the accretion rate implied by the bolometric luminosity of the AGN is so low compared to

the available gas supply (e.g. Ho 2009). The second unsolved problem is how does the gas lose angular momentum in order to be accreted (e.g. Begelman 1994; Proga & Begelman 2003, and references therein). Both of these difficulties can be solved simultaneously if the source of the inflowing material is zero angular momentum gas resulting from stellar-mass loss satisfying;

$$r \times p = 0 \tag{12}$$

where $r$ is the radius vector centered on the BH and $p$ is the linear momentum of the gas escaping from the stars. Only a small fraction of the stellar mass loss gas is expected to have zero angular momentum and naturally explains why the accretion rate is observed to be low, $\leq 0.1$ $M_\odot$ $yr^{-1}$, in M81 (Devereux & Shearer 2007), NGC 3998 (Devereux 2011a), NGC 4203 (Devereux 2011b) and NGC 3227 studied here. For these objects, not only is the accretion rate implied by the bolometric luminosity of the AGN low, the accretion rate is *actually observed to be low* and the explanation offered here for that observation is that the BH accretes *only the fraction of gas produced by stellar mass loss that has zero angular momentum.*

### 4.8. Ouflow?

Both Denney et al. (2009) and Winter, Veilleux, McKernan & Kallman (2011) have raised the possibility of outflowing gas *at* and *inside*[6] the reverberation radius in NGC 3227. However, the low Eddington ratio dictates that radiation pressure acting on the ionized gas fails to overcome the gravitational force by a factor of $\sim 250$. Furthermore, a dust driven outflow (Fabian, Celotti, & Erlund 2006) seems unlikely as the dust reverberation radius ($\sim$20 l.d., Suganuma et al. 2006) lies well beyond the gas reverberation radius ($\sim$4 l.d., Denney et al. 2009) as illustrated in Figure 8. Additionally, any advection driven outflow is predicted to occur on a size scale comparable to $r_g$ (Narayan, Kato & Honma 1997) which is $\sim$1000 times smaller than the gas reverberation radius in NGC 3227. Thus, it is incumbent on proponents of outflow to identify a viable mechanism that operates over $4\pi$ steradians and is able to thwart the ballistic pressure of the inflow, estimated to be $\sim 0.4$ erg/cm$^3$ at the gas reverberation radius and increasing as $r^{-2}$ towards the central BH.

---

[6]Based on the ionization parameter measured for the O VII and O VIII absorption lines by Winter, Veilleux, McKernan & Kallman (2011)

### 4.9. Summary

Collectively, the results presented here for NGC 3227 challenge many preconceived notions concerning the nature of BLRs in active galactic nuclei. Firstly, there are quite likely no *broad line clouds* but rather ionized gas *filaments*. Secondly, the BLR is *not small*, it is just *perceived* to be small. Thirdly, the single peak broad Balmer emission lines, which are by far the most common type of broad emission line seen in AGNs, are quite likely the signature of a large, $\sim$ parsec sized, *ballistic inflow* not a Bondi flow. Fourthly, the observed mass inflow rate *is* commensurate with that required to power the AGN in terms of radiatively inefficient accretion. However, it remains to be determined to what extent these findings for NGC 3227 apply to more luminous AGNs. Nevertheless, the picture emerging from analysis of *HST*/STIS observations, to date, is that the BLR of LLAGN are very different from each other with no evidence to support the notion of a *standard, classical* or *normal* BLR.

## 5. Conclusions

Spectroscopic observations of NGC 3227 with the *Hubble Space Telescope (HST)* have revealed a time variable single-peak broad H$\alpha$ emission line profile which has been successfully modeled as a steady state inflow. The *perceived* dimensions of the BLR correspond to an outer radius of $\sim$ 60 l.d. and an inner radius of $\sim$ 4 l.d. coinciding with the gas reverberation radius. However, the *perceived* small size for the BLR is an illusion, a consequence of the fact that the emitting region is ionization bounded at the outer radius and diminished by Doppler broadening at the inner radius. The actual dimensions of the inflow are likely much larger and remain to be determined. If the gas density is high, $\geq 10^6$ cm$^{-3}$, as suggested by the absence of similarly broad [O I] and [O III] emission lines, then the luminosity in the broad H$\alpha$ emission line observed in the year 2000 leads to a steady state inflow rate $\sim 1 \times 10^{-2}$ M$_\odot$ yr$^{-1}$ which is sufficient to explain the X-ray luminosity of the AGN, if the AGN is powered by radiatively inefficient accretion.

This research has made extensive use of the NASA Astrophysics Data System, the Atomic Line List, http://www.pa.uky.edu/$\sim$peter/newpage/ and a variety **STSDAS** tasks. Support for Program number HST-AR-11752.01-A was provided by NASA through a grant from the Space Telescope Science Institute, which is operated by the Association of Universities for Research in Astronomy, Incorporated, under NASA contract NAS5-26555.

*Facilities:* HST (STIS)

## REFERENCES

Begelman, M. C., in Mass-Transfer Induced Activity in Galaxies, proceedings of the Conference held at the University of Kentucky, Lexington, April 26-30, 1993. Edited by Isaac Shlosman. Cambridge: Cambridge University Press, 1994, p.23

Bondi, H., 1952, MNRAS, 112, 195

Bower, G.A., Wilson, A.S., Heckman, T.M., & Richstone, D.O.,1996, AJ, 111, 1901

Capriotti, E., Foltz, C., & Byard, P., 1980, ApJ, 245, 396

Chen, K., & Halpern, J.P., 1989, ApJ, 344, 115

Cohen, R.D., 1983, ApJ, 273, 489

Collin, S., Kawaguchi, T., Peterson, B.M., & Vestergaard, M., 2006, å, 456, 75

Crenshaw, D.M., Kraemer, S.B., Bruhweiler, F.C., & Ruiz, J.R., 2001, ApJ, 555, 633

Davies, R.I., et al., 2006, ApJ, 646, 754

Denney, K.D., et al., 2009, ApJ, 704, 80

Denney, K.D., et al., 2010, ApJ, 721, 715

Devereux, N., 2011, ApJ, 727, 93

Devereux, N., 2011, ApJ, 743, 83

Devereux, N.A., Becklin, E.E., & Scoville, N.Z., 1987, ApJ, 312, 529

Devereux, N., & Shearer, A., 2007, ApJ, 671, 118

Edelson, R.A.,& Krolik, J.H., 1988, ApJ, 333, 646

Eracleous, M., & Halpern J.P., 2001, ApJ, 554, 2406

Fabian, A.C., Celotti, A. & Erlund, M.C., 2006, MNRAS, 373, L16

Filippenko, A.V., & Halpern, J.P., 1984, ApJS, 285, 458

Ho, L.C., 2009, ApJ, 699, 626

Ho, L.C., Filippenko, A.V., Sargent, W.L.W., & Peng, C.Y., 1997, ApJS, 112, 391

Horne, K., Peterson, B., Collier, S., & Netzer, H., 2004, PASP, 116, 465

Hicks, E.K.S., & Malkan, M.A., 2008, ApJS, 174, 31

Kaspi, S., Maoz, D., Netzer, H.,Peterson, B.M., Vestergaard, M., & Jannuzi, B.T., 2005, ApJ, 629, 61

King, A., & Pounds, K., 2003, MNRAS, 347, 657

Kewley, L.J., Groves, B., Kauffmann, G., & Heckman, T., 2006, MNRAS, 372, 961

Lacy, J. H., Achtermann, J. M., & Serabyn, E., 1991, ApJ, 380, 71

Mathews, W.G., & Ferland, G.J., 1987, ApJ, 323, 456

Merloni, A., Heinz, S., & Di Matteo, T., 2003, MNRAS, 345, 1057

Makowitz, A., et al., 2009, ApJ, 691, 922

Murry, N., & Chiang, J., 1997, ApJ, 474, 91

Narayan, R., Kato, S., & Honma, F., 1997, ApJ, 476, 49

Noel–Storr et al., 2003, ApJS, 148, 419

Onken, C.A., et al., 2004, ApJ, 615, 645

Peterson, B., 1993, PASP, 105, 247

Peterson, B.M., Crenshaw, D.M, & Meyers, K.A., 1985, ApJ, 298, 283

Peterson, B.M., et al., 2004, ApJ, 613, 682

Proga, D., & Begelman, M.C., 2003, ApJ, 592, 767

Proffitt, C., et al., 2010, STIS Instrument Handbook, Version 9.0, (Baltimore: STScI).

Robinson, A., & Perez, E., MNRAS, 244, 138

Suganuma, M., et al., 2006, ApJ, 639, 46

Shlosman, I., Vitello, P.A., & Shaviv, G., 1985, ApJ, 294, 96

Storchi-Bergmann, The Monster's Fiery Breath: Feedback in Galaxies, Groups, and Clusters. AIP Conference Proceedings, Volume 1201, pp. 88-91 (2009).

Storchi-Bergmann, T., Eracleous, M., Ruiz, M.T., Livio, M., Wilson, A. S., Filippenko, A. V., 1997, ApJ, 489, 87

Tully, R.B., 1988, *Nearby Galaxies Catalog*, Cambridge University Press.

Vasudevan, R.V., & Fabian, A.C., 2009, MNRAS, 392, 1124

Walsh, J.L., 2008, ApJ, 136, 1677

Welsh, W.F., & Horne, K., 1991, ApJ, 379, 586

Winge et al., 1995, ApJ, 445, 680

Winter, L.M., Veilleux, S., McKernan, B., & Kallman, T.R., 2011, ApJ, 745, 107

Xu, Y-D., 2011, ApJ,739 64

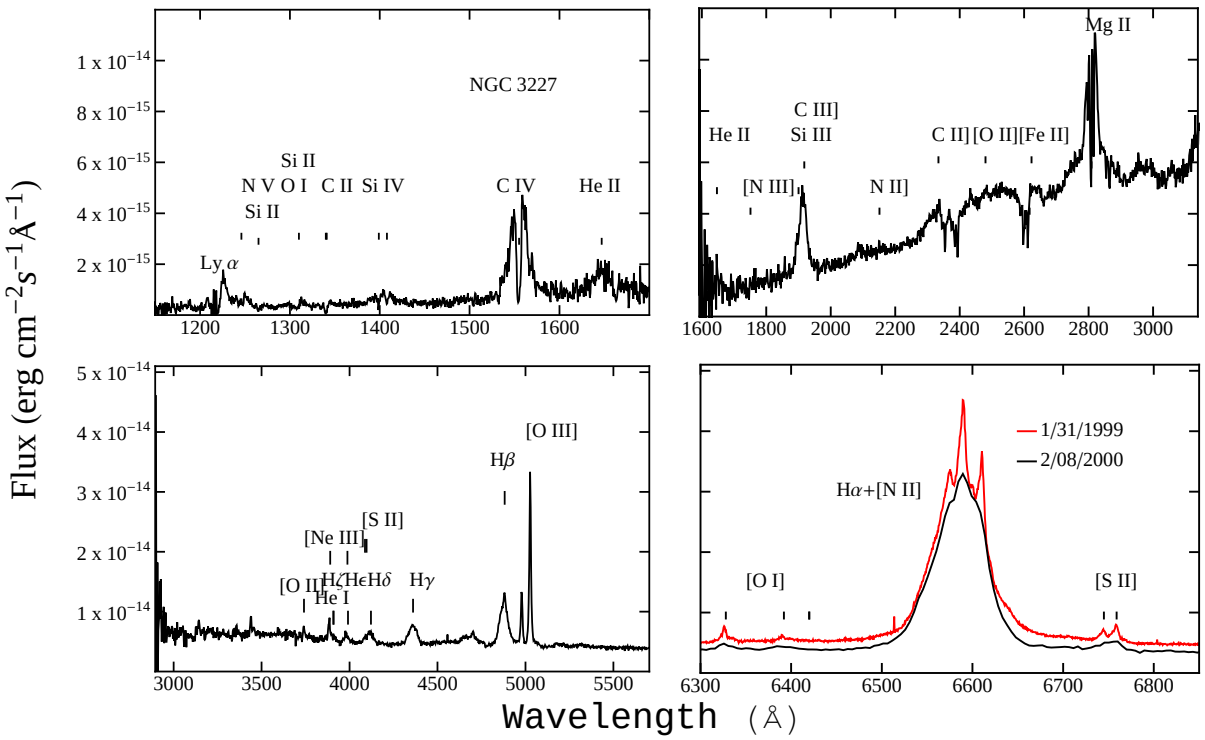


Fig. 1.— Visual and UV spectra of NGC 3227 as seen through the following gratings: *Top left panel*: G140L. *Top right panel*: G230L. *Lower left panel*: G430L. *Lower right panel*: G750M. Red line shows data obtained under PID 7403. Black lines for all panels show data obtained under PID 8479.

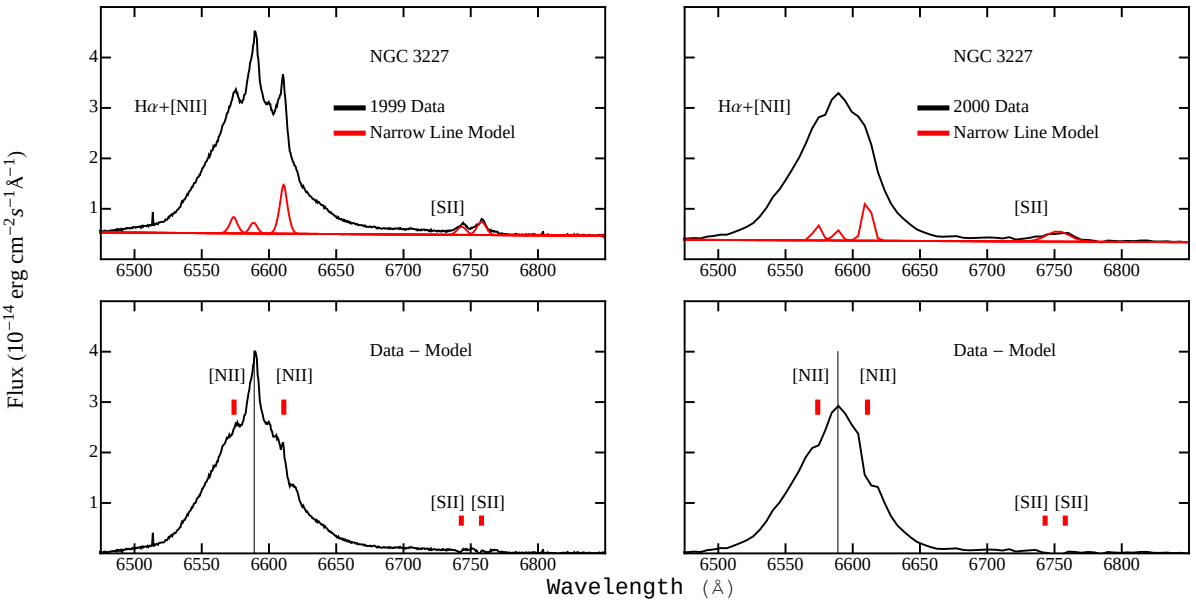


Fig. 2.— Broad H$\alpha$ emission line in NGC 3227 observed in 1999 with G750M (*Left panels*) and 2000 with G750L (*Right panels*). *Top panels*: The observed spectrum is shown in black and a model for the forbidden lines is shown in red (see also Table 2). *Lower panels*: The broad H$\alpha$ emission line profile after the forbidden lines have been subtracted. The central wavelengths of the subtracted lines are indicated in red. The vertical black line corresponds to the observed (redshifted) central wavelength of the H$\alpha$ line

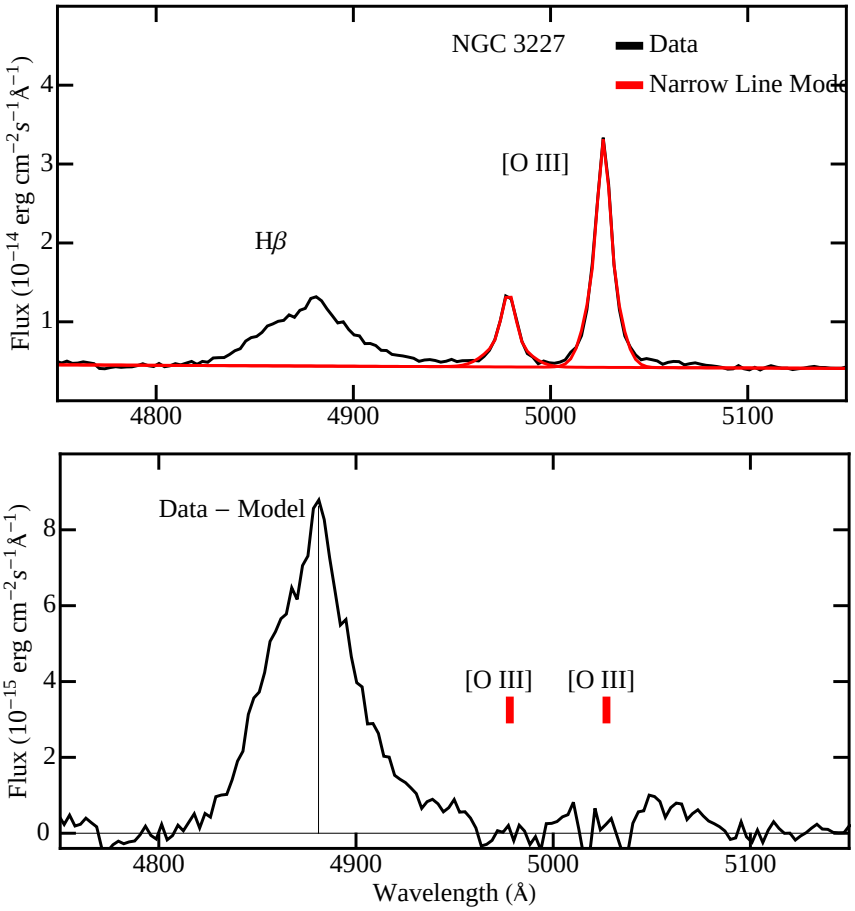


Fig. 3.— Broad H$\beta$ emission line in NGC 3227 observed in 2000. *Top panel*: The observed spectrum is shown in black and a model for the forbidden lines is shown in red (see also Table 3). *Lower panel*: The broad H$\beta$ emission line profile after the forbidden lines have been subtracted. The central wavelengths of the subtracted lines are indicated in red. The vertical black line corresponds to the observed (redshifted) central wavelength of the H$\beta$ line

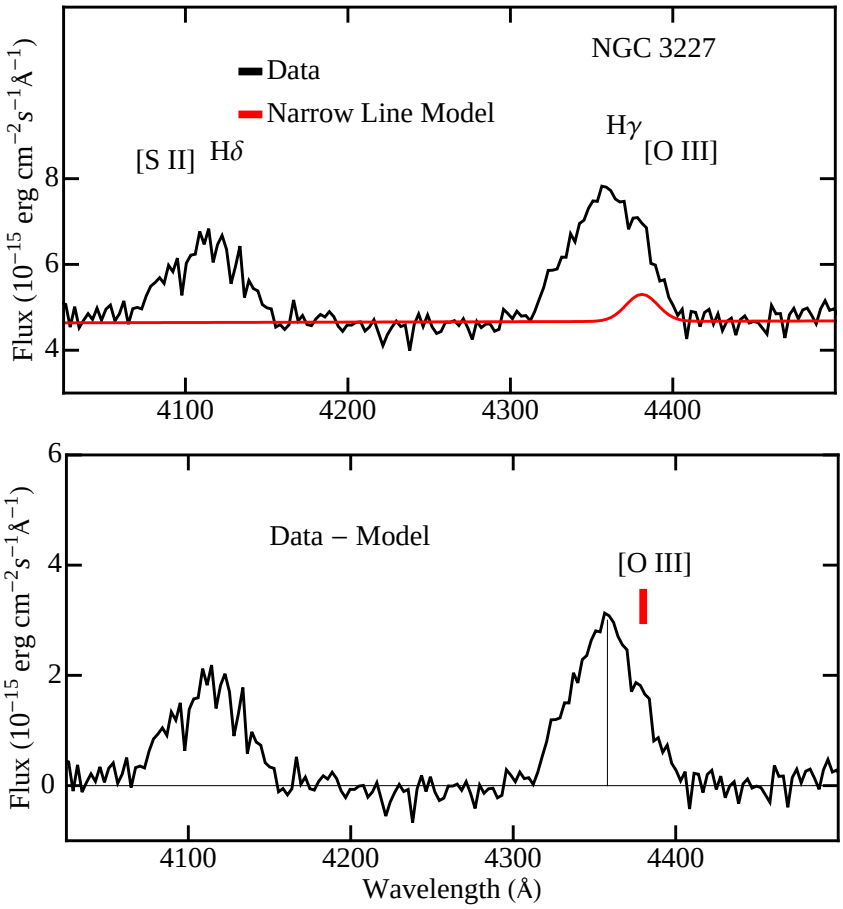


Fig. 4.— Broad H$\gamma$ emission line in NGC 3227 observed in 2000. *Top panel*: The observed spectrum is shown in black and a model for the forbidden line is shown in red (see also Table 3). *Lower panel*: The broad H$\gamma$ emission line profile after the forbidden line has been subtracted. The central wavelength of the subtracted line is indicated in red. The vertical black line corresponds to the observed (redshifted) central wavelength of the H$\gamma$ line

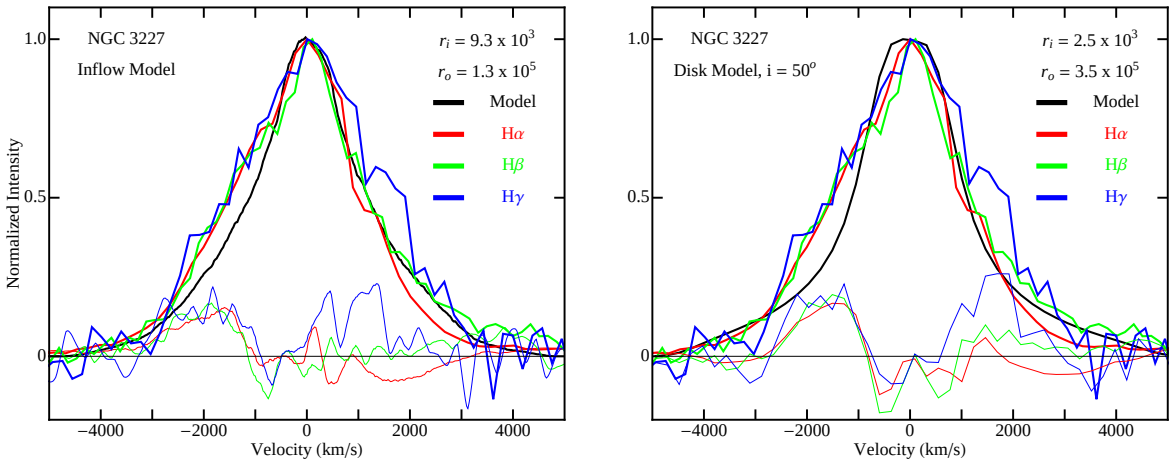


Fig. 5.— Model representation of the broad Balmer lines observed with the G750L grating (Left panel) in terms of a spherically symmetric inflow and (Right panel) in terms of a relativistic accretion disk. The observed H$\alpha$, H$\beta$ and H$\gamma$ emission lines are shown in red, green and blue, respectively. The inflow and disk models are shown in black. The inner, $r_i$, and outer radii, $r_o$, are indicated in units of gravitational radii, $r_g$. Residuals for each profile are plotted as thinner colored lines.

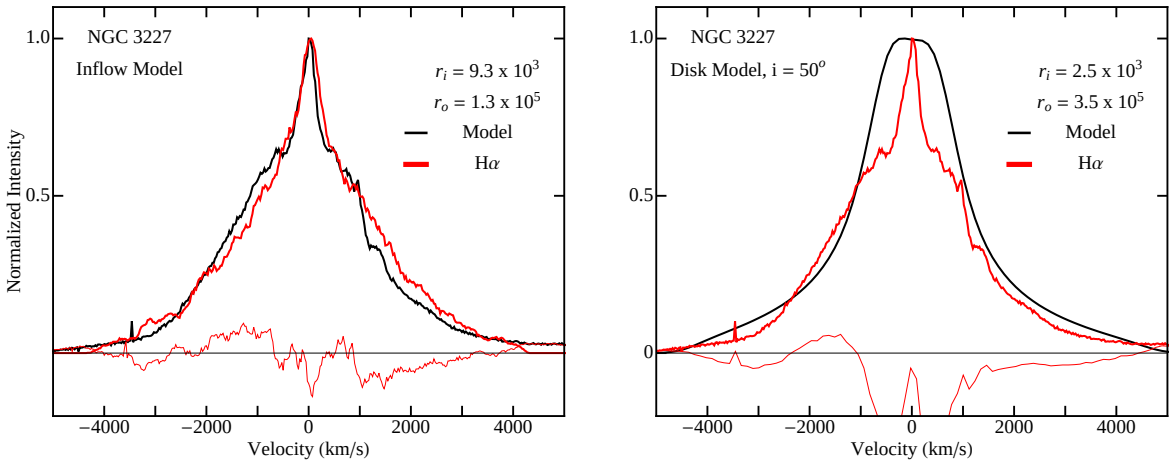


Fig. 6.— Model representation of the broad H$\alpha$ line observed with the G750M grating (Left panel) in terms of a spherically symmetric inflow and (Right panel) in terms of a relativistic accretion disk. The observed H$\alpha$ emission line is shown in red. The inflow and disk models are shown in black. The inner, $r_i$, and outer radii, $r_o$, are indicated in units of gravitational radii, $r_g$. Residuals for each profile are plotted as thinner red lines.

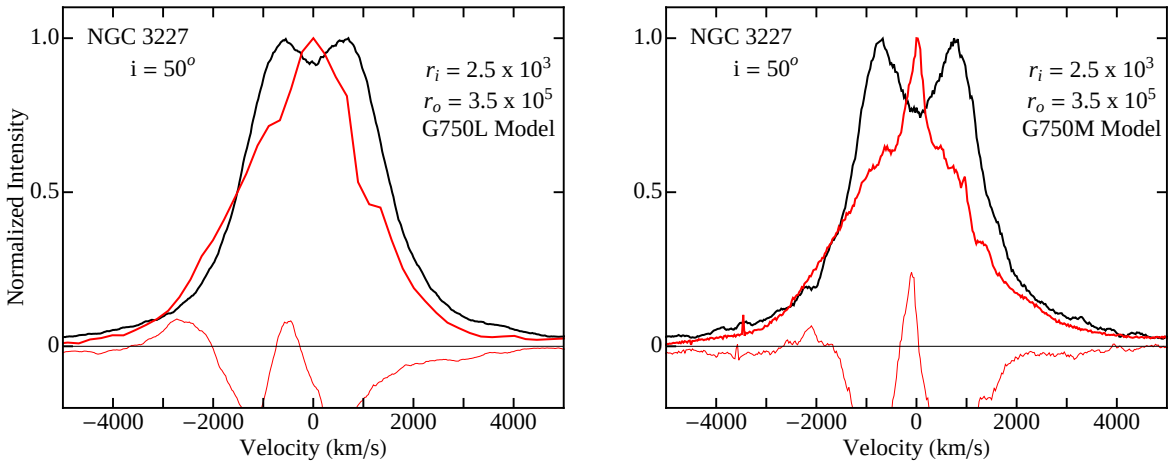


Fig. 7.— Non-relativistic discrete disk model representation of the broad H$\alpha$ line illustrating the effect of spectral resolution. (Left panel) simulated observation with the G750L grating. (Right panel) simulated observation with the G750M grating. The observed H$\alpha$ emission lines are shown in red. The disk models are shown in black. The inner, $r_i$, and outer radii, $r_o$, are indicated in units of gravitational radii, $r_g$. Residuals for each profile are plotted as thinner red lines.

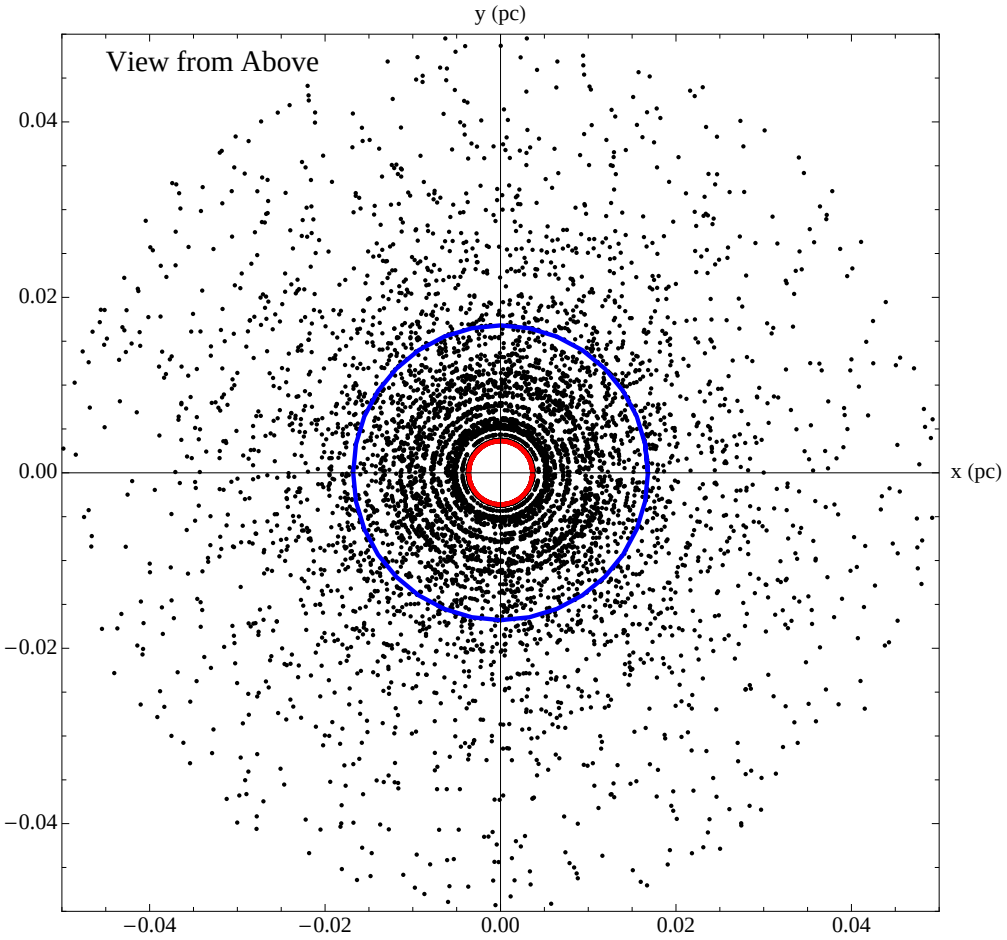


Fig. 8.— Visualization of the model inflow. The red ring identifies 8% of the points representing the percentage of the total broad line flux which is observed to respond to time-variable illumination from the central AGN (Denney et al. 2009). The blue ring identifies the $K$–band reverberation radius (Suganuma et al. 2006). This figure is the first frame in an animation that is accessible in the electronic edition of the *Astrophysical Journal*.

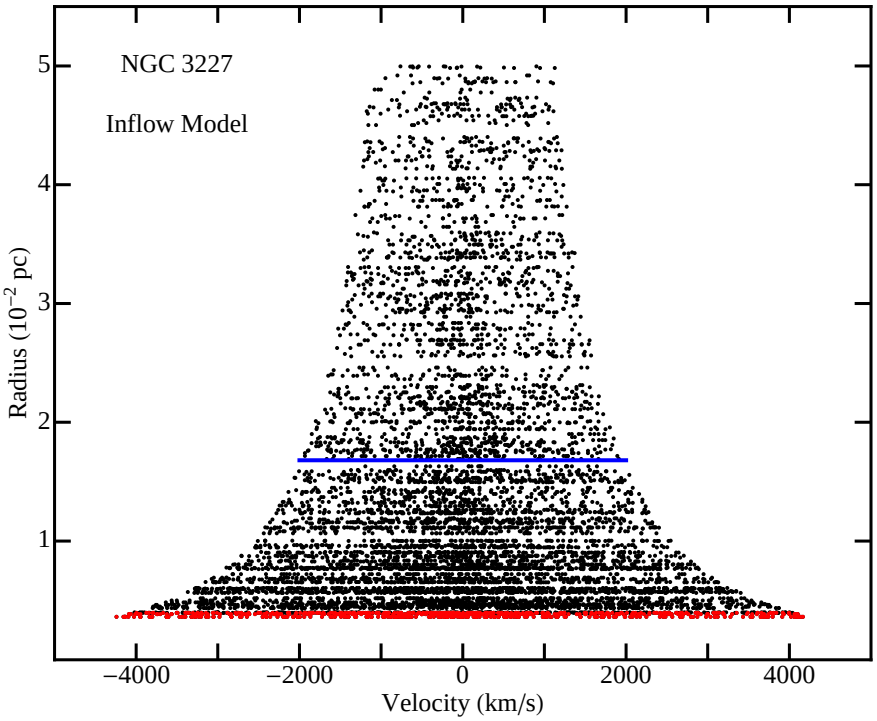


Fig. 9.— The number density of points in the model inflow. Red line identifies 8% of the points representing the percentage of the total broad line flux which is observed to respond to time-variable illumination from the central AGN (Denney et al. 2009). The blue line identifies the $K$-band reverberation radius (Suganuma et al. 2006). The corresponding model broad H$\alpha$ profile, shown in Figures 5 and 6, are produced by summing the points vertically.

Table 1. NGC 3227 Spectral Datasets

| PID | Observation Date | Grating | Spectral Range Å | Slit arc sec | Dispersion Å/pixel | Plate Scale arc sec/pixel | Integration Time s | Datasets |
|---|---|---|---|---|---|---|---|---|
| (1) | (2) | (3) | (4) | (5) | (6) | (7) | (8) | (9) |
| 7403 | 1-31-1999 | G750M | 6295 – 6867 | 52 x 0.2 | 0.56 | 0.05 | 1890 | o57204040 |
| 8479 | 2-8-2000 | G230L | 1570 – 3180 | 52 x 0.2 | 1.58 | 0.025 | 1612 | o5kp01010 |
| 8479 | 2-8-2000 | G430L | 2900 – 5700 | 52 x 0.2 | 2.73 | 0.05 | 120 | o5kp01020 |
| 8479 | 2-8-2000 | G140L | 1150 – 1736 | 52 x 0.2 | 0.6 | 0.024 | 2132 | o5kp01030 |
| 8479 | 2-8-2000 | G750L | 5236 – 10266 | 52 x 0.2 | 4.92 | 0.05 | 120 | o5kp01040 |

Table 2. Emission Line Parameters for the G750M Nuclear Spectrum Obtained 1–31–1999[a]

| Line | Central Wavelength[b] Å | Flux[c] $10^{-15}$ erg cm$^{-2}$ s$^{-1}$ | FWHM kms$^{-1}$ |
|---|---|---|---|
| (1) | (2) | (3) | (4) |
| [O I] | 6326 ± 1 | 12.9 ± 0.7 | 298 ± 24 |
| [O I] | 6390 ± 1 | 6.3 ± 0.9 | 298 ± 52 |
| [N II] | 6574 ± 3 | 23.7 ± 1.7 | 357 |
| H$\alpha$ (broad)[d] | 6588 | 2150 ± 1 | 2147 ± 100 |
| H$\alpha$ (broad)[e] | 6588 | 1900 ± 3 | 2676 ± 200 |
| H$\alpha$ (narrow) | 6588 ± 3 | 15.0 | 357 |
| [N II] | 6610 ± 1 | 71.5 ± 5[f] | 357 |
| [S II] | 6744 ± 1 | 20.8 ± 2[g] | 357 ± 47 |
| [S II] | 6758 ± 1 | 26.6 ± 2[g] | 357 ± 34 |

[a]Table entries that do not include uncertainties are fixed parameters.

[b]Observed wavelength

[c]Continuum subtracted but not corrected for dust extinction. Model dependent systematic uncertainties introduce an additional $\sim$ 3% error.

[d]1999

[e]Observation date: 2–8–2000, G750L

[f]The [N II] emission line flux is chosen so as to not over-subtract the broad H$\alpha$ emission line profile. The [N II] line shape is modeled using two gaussian components; one of width 357 km/s and another of width 151 km/s contributing 10% of the total emission line flux.

[g]The [S II] emission lines are unresolved in the lower resolution spectrum obtained with the G750L grating on 2–8–2000. However, the sum of the flux in the two lines then was (43.7 ± 6) $\times 10^{-15}$ erg cm$^{-2}$ s$^{-1}$ which concurs with the sum of the flux in the [S II] lines measured on 1–31–1999.

Table 3. Emission Line Parameters for the G430L Nuclear Spectrum Obtained 2–8–2000[a]

| Line | Central Wavelength[b] Å | Flux[c] $10^{-14}$ erg cm$^{-2}$ s$^{-1}$ | FWHM kms$^{-1}$ |
|---|---|---|---|
| (1) | (2) | (3) | (4) |
| H$\gamma$ (broad) | 4356 | 14.9 ± 0.1 | 2747 ± 300 |
| [O III][d] | 4381 | $\leq$ 1.5 | 1576 |
| H$\beta$ (broad) | 4882 | 47.4 ± 0.01 | 2794 ± 300 |
| [O III][e] | 4978 ± 1 | 12.93 ± 1.0 | 1576 |
| [O III][e] | 5027 ± 1 | 37.61 ± 1.0 | 1576 ± 186 |

[a]Table entries that do not include uncertainties are fixed parameters.

[b]Observed wavelength

[c]Measured within a 0.2″ x 0.35″ aperture. Continuum subtracted but not corrected for dust extinction.

[d]The [O III] emission line flux is chosen so as to not over-subtract the broad H$\gamma$ emission line profile

[e]The [O III] emission lines are modeled using two gaussian components; one of width 1576 km/s and another gaussian of width 556 km/s contributing 55% of the total emission line flux.

Table 4. Stellar Mass Model

| r pc (1) | r mas (2) | M(r)[a] $10^6$ $M_\odot$ (3) | $\rho$(r)[b] $10^6 M_\odot/pc^3$ (4) |
|---|---|---|---|
| 1 | 9.90 | 5.56 | 1.3 |
| 0.5 | 4.90 | 1.63 | 3.1 |
| 0.25 | 2.47 | 0.48 | 7.3 |
| 0.125 | 1.24 | 0.14 | 16.5 |
| 0.0625 | 0.62 | 0.04 | 36.2 |

[a]Enclosed stellar mass calculated by integrating the $H$-band surface brightness profile parameterized by Hicks & Malkan (2008), adopting an $H$-band mass-to-light ratio M/L = 0.7 and +3.65 for the absolute $H$-band magnitude for the Sun (Devereux, Becklin & Scoville 1987).

[b]Stellar mass density